

Chemical potential and quantum Hall ferromagnetism in bilayer graphene mapped using double bilayer heterostructures

Kayoung Lee¹, B. Fallahazad¹, J. Xue¹, T. Taniguchi², K. Watanabe², E. Tutuc¹

¹*Microelectronics Research Center, The University of Texas at Austin, 10100 Burnet Rd., Austin, TX
78758, USA*

²*National Institute for Materials Science, 1-1 Namiki Tsukuba Ibaraki 305-0044, Japan*

A key property of an electron system is the chemical potential, or Fermi energy. This property captures the physics of both the energy-momentum band structure, as well as interaction-induced corrections to the single particle energy. We study the electron transport in double bilayer graphene heterostructures, consisting of two Bernal stacked bilayer graphene flakes separated by a hexagonal boron nitride dielectric layer. By using the top layer as a resistively detected Kelvin probe, we map the chemical potential (Fermi energy) in the opposite (bottom) layer as a function of density and magnetic field. At zero magnetic field the chemical potential reveals a super-linear dependence on electron density, consistent with the non-parabolic energy-momentum dispersion, as well as an electric field induced gap opening at the charge neutrality point. The measured chemical potential has values larger than tight-binding calculations, a result attributed to electron-electron interaction. In perpendicular magnetic fields the samples display quantum Hall states (QHS) at all integer filling factors, which undergo transitions as a function of magnetic and transverse electric fields, associated with the interplay between Landau level spin and valley degrees of freedom. The chemical potential dependence on filling factor provides a direct measurement of the orbital Landau levels energies, as well as the gaps of interaction-induced QHSs.

Bilayer graphene represents a peculiar two-dimensional electron system^{1,2}, possessing a bandgap and energy-momentum dispersion that can be tuned by an applied transverse electric field^{3,4}. In high magnetic fields, electron-electron interaction coupled with the spin and valley degrees of freedom can lead to a diverse set of quantum Hall states¹⁻⁹. Thermodynamic measurements of the chemical potential or the density of states are fundamental to understanding the bilayer graphene electronic properties¹⁰⁻¹³. Such measurements however, tend to be stymied by the reduced sample dimensions. Global measurements of the density of states (DOS) in bilayer graphene performed through compressibility measurements¹⁰ reported the DOS modulation associated with four-fold, spin and valley degenerate Landau levels, while local compressibility measurements in single-gated suspended bilayer graphene samples revealed broken symmetry QHSs¹³.

The samples investigated in this study consist of two Bernal stacked bilayer graphene layers, separated by a thin hexagonal boron nitride (hBN) layer (Fig. 1a). The samples are fabricated using a sequence of mechanical exfoliation, dry-transfer, and alignment with a pre-existing device similarly to refs 14, 15. The bottom bilayer graphene is supported by a thick (30-50 nm) hBN substrate, mechanically exfoliated on a SiO₂/Si substrate. A relatively thin (2-6 nm) interlayer hBN layer is then transferred and aligned with the bottom layer, followed by the top bilayer graphene transfer. Each bilayer graphene is patterned into a multi-terminal Hall bar, and an etch-through of the two layers ensures the Hall bar edges are aligned. A false-color optical micrograph of one of the devices examined in this study is shown in Fig. 1b inset. The layer resistances are measured as a function of back-gate (V_{BG}), and inter-layer bias applied to the top layer (V_{TL}) using small signal, low frequency lock-in techniques. Three samples, labelled #1, #2, and #3, were investigated in this study. The bottom bilayer graphene in all the samples have

mobilities ranging between 100,000 – 290,000 cm²/Vs, while the top bilayer graphene has a lower mobility presumably because it is exposed.

Figure 1b and 1c show contour plots of the top (panel b), and bottom (panel c) bilayer resistances as a function of V_{BG} and V_{TL} , measured at a temperature $T = 1.4$ K. The top (n_T) and bottom (n_B) layer densities, which in turn control the layer resistances, depend on V_{BG} and V_{TL} as follows¹⁶:

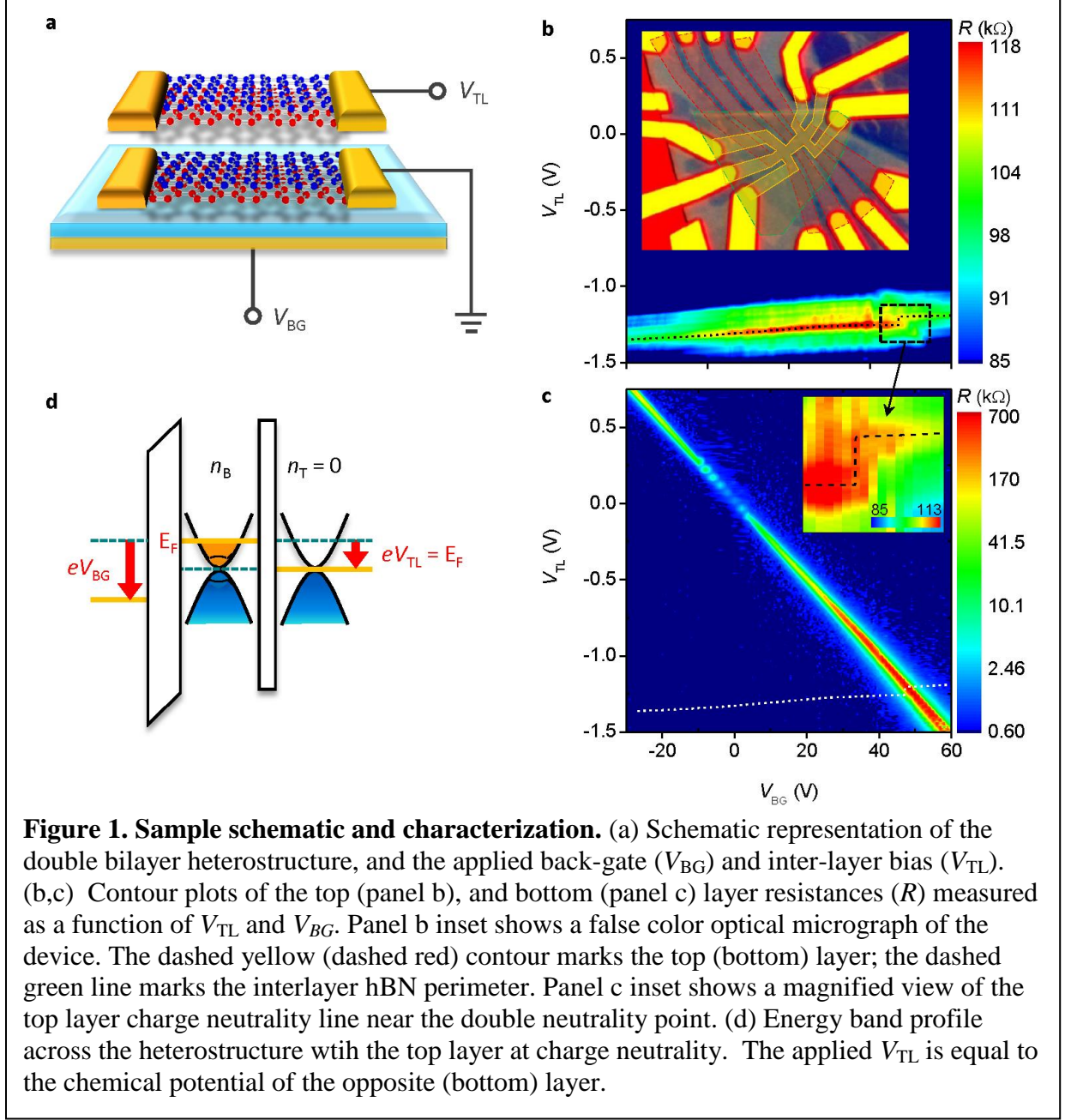
$$eV_{BG} = e^2(n_B + n_T)/C_{BG} + \mu_B \quad (1)$$

$$eV_{TL} = -e^2n_T/C_{int} - \mu_T + \mu_B \quad (2)$$

Here, C_{BG} and C_{int} represent the bottom and interlayer dielectric capacitances, while μ_T and μ_B represent the chemical potentials (Fermi energies) of the top and bottom layers, respectively; e is the electron charge. Equation (1) is derived assuming the applied V_{BG} is the sum of the electrostatic potential drop on the bottom dielectric and the Fermi energy of the bottom layer. Similarly, in Eq. (2) the applied V_{TL} is the sum of the electrostatic potential drop on the interlayer dielectric and the Fermi energies of the two layers. We note that μ and n are positive (negative) for electrons (holes), and V_{BG} and V_{TL} in Eqs. (1) and (2) are referenced with the bias values at which both layers are charge neutral, i.e. at the double neutrality point (DNP). Using Eqs. (1) and (2), the externally applied transverse electric field (E) across the bottom bilayer writes as follows:

$$E = en_B/2\varepsilon_0 + en_T/\varepsilon_0 + E_0 \quad (3)$$

ε_0 is the vacuum permittivity, n_B and n_T are determined using Eqs. (1) and (2), and E_0 is an additive constant which allows for a finite transverse electric field at the DNP, associated with the unintentional doping of the top layer.

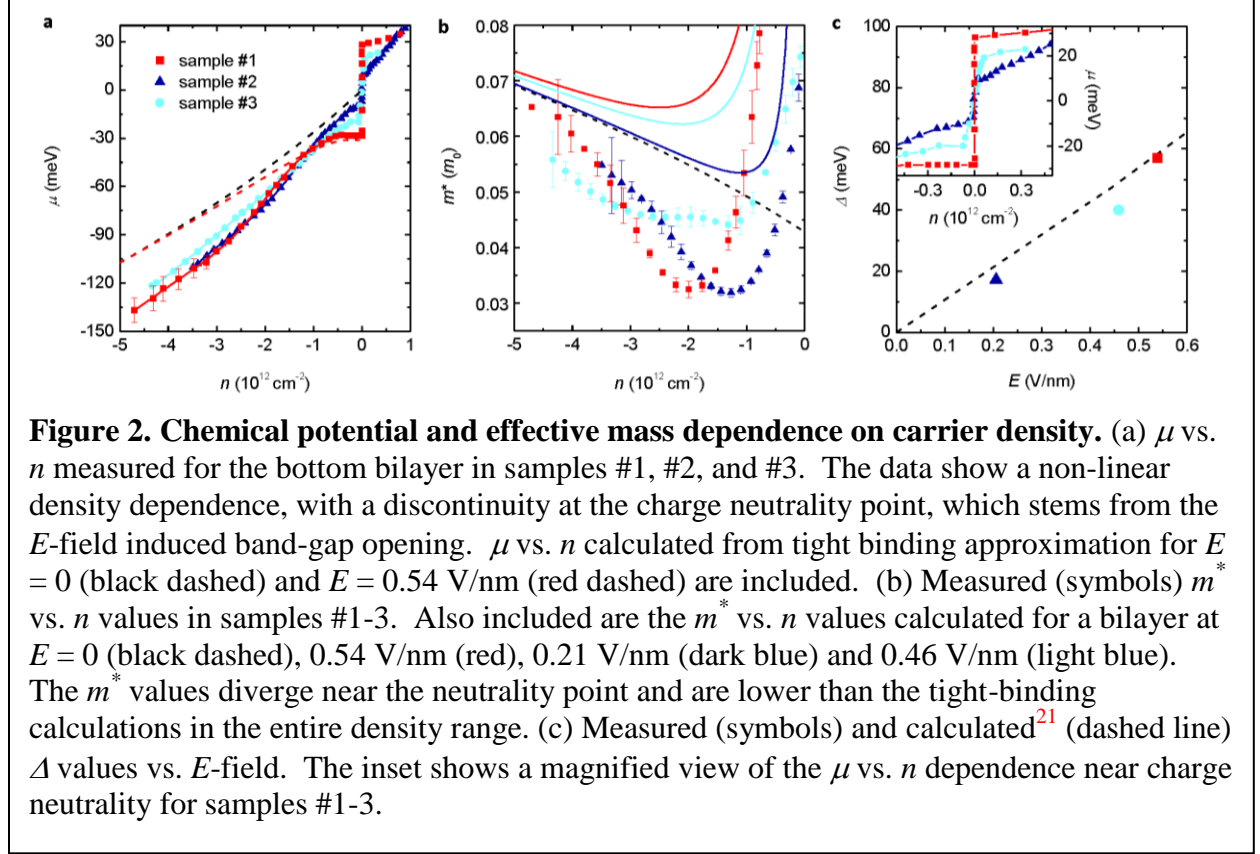


The bottom bilayer density and resistance dependence on V_{BG} and V_{TL} in Fig. 1c is similar to that of a dual gated bilayer¹⁶⁻¹⁹, where the charge neutrality point has a linear dependence on V_{BG} and V_{TL} , with a slope controlled by the inter-layer and bottom dielectric capacitances. In addition to changing the layer density, the applied V_{BG} and V_{TL} also change the transverse electric field across the bilayers. Along the charge neutrality line of the bottom bilayer, the

resistance is minimum at zero transverse electric field, and increases with the E -field thanks to the E -field-induced band gap of bilayer graphene. By comparison to the bottom bilayer, the top bilayer graphene resistance has weak dependence on V_{BG} thanks to the screening by the bottom bilayer, and is controlled primarily by V_{TL} . An important observation can be made by examining the conditions in which the top layer is at charge neutrality. Setting $n_T = 0$ in Eq. (2) yields $eV_{TL} = \mu_B$, which implies that the interlayer bias required to bring the top graphene to charge neutrality is simply the chemical potential of the bottom graphene (Fig. 1d) in units of eV¹⁶. Furthermore, using Eq. (1) the n_B values along the top graphene neutrality line (dotted line in Fig. 1b and 1c) are $n_B = C_{BG}(V_{BG} - V_{TL})/e$. Consequently, the bottom bilayer chemical potential can be fully mapped as a function of density.

Figure 2a shows the bottom layer chemical potential (μ) vs. density (n) determined as described above in the bottom layer of samples #1, #2, and #3. Because the top layer residual doping varies in these samples, the transverse E -field across the bottom bilayer at the DNP is finite, and different in the three samples examined here (0.54 V/nm, 0.21 V/nm, and 0.46 V/nm for samples #1, #2, and #3, respectively). Several observations can be made by examining Fig. 2a data. First, the chemical potential shows a clear discontinuity as n changes sign, evincing a gap (Δ) between the valence and conduction bands, associated with the E -field induced band-gap in bilayer graphene^{3,4}. Second, the μ vs. n dependence is nonlinear, with a marked dependence on the E -field at low densities. Such dependence contrasts the $\mu \propto \sqrt{n}$ dependence of monolayer graphene², or the linear $\mu \propto n$ dependence expected for massive 2D system, evincing a strongly non-parabolic energy momentum dispersion^{3,10,11,20}. For comparison, Fig. 2a includes the μ vs. n dependence calculated for the lowest energy band in bilayer graphene within a tight binding approximation^{3,21} for $E = 0$ and $E = 0.54$ V/nm; the latter value corresponds to the E -field

across the bottom layer at DNP in sample #1. The calculations use the non-interacting in-plane velocity $v = 8.4 \times 10^5$ m/s, inter-layer hopping $\gamma_1 = 0.34$ eV²¹, and neglect trigonal warping, which is relevant only at very low densities.



The experimental μ values are rather insensitive to the E -field at high carrier densities, consistent with tight binding theoretical results³. However the experimental μ values are larger than the band calculations, particularly at high densities, a finding explained by the interaction-induced renormalization of electron energies^{22,23}. Figure 2a data allow us to extract the density of states effective mass (m^*), defined as $m^* = (\pi\hbar^2/2) \cdot (d\mu/dn)^{-1}$. Figure 2b shows the m^* vs. n data in samples #1, #2, and #3. For comparison we include the tight binding m^* vs. n dependence at $E = 0.54$ V/nm (red), 0.21 V/nm (dark blue), and 0.46 V/nm (light blue), the E -field values across the bottom bilayer at DNP in our samples #1, #2, and #3, respectively, and

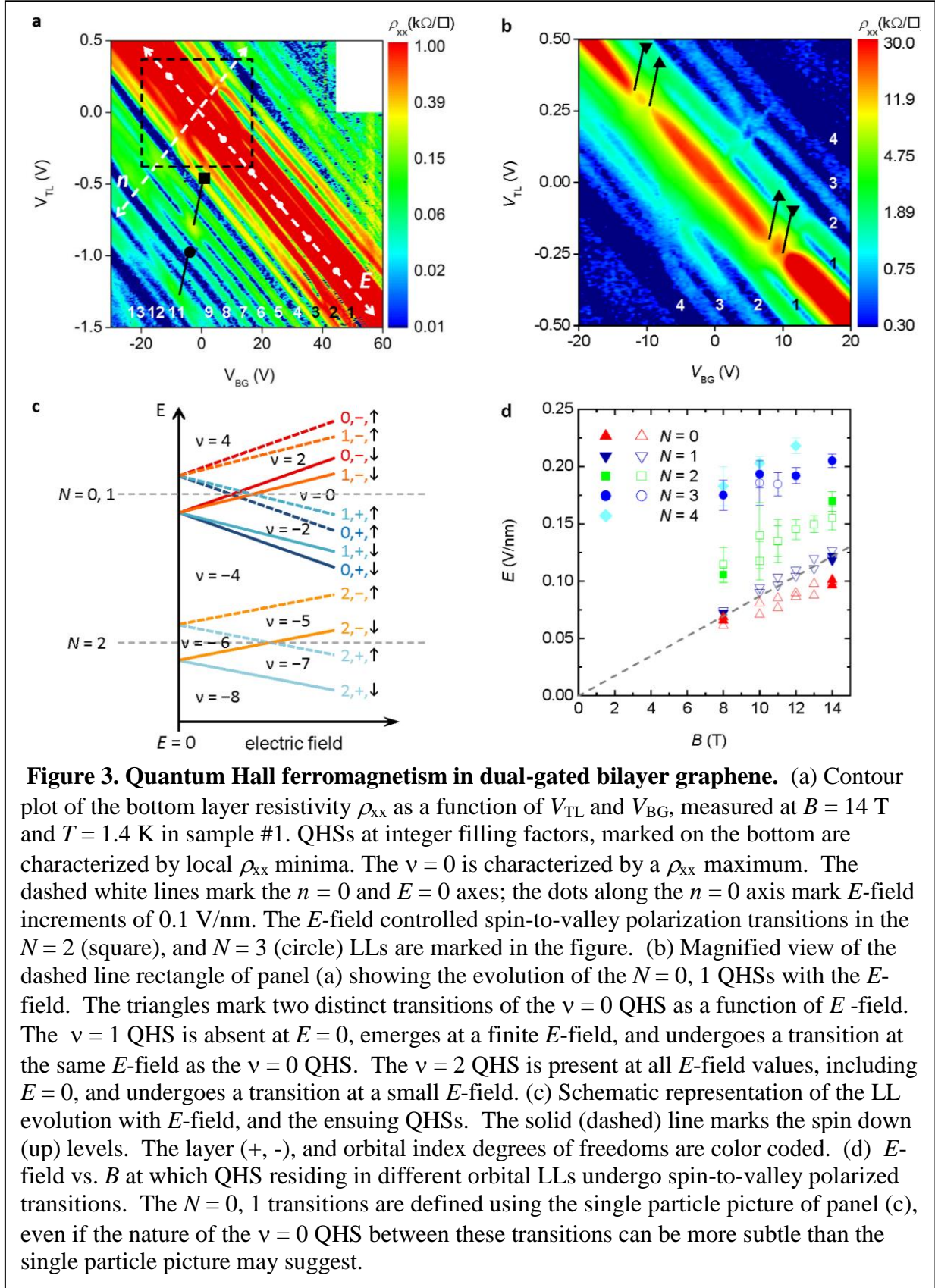
also at $E = 0$ (black)³. The non-linearity of the μ vs. n data translates into an effective mass with a strong, non-monotonic dependence on density. At low densities the measured m^* increases with the transverse E -field, and shows a divergence as a function of n in the proximity of the neutrality point. Note that the bottom bilayer is under a finite E -field at DNP, and m^* at the band edge increases with the E -field as the mexican hat structure evolves³. The non-monotonic m^* vs. n dependence is consistent with the tight-binding calculations, albeit with lower values in the entire density range, because of the interaction-induced renormalization.

One peculiar property of bilayer graphene is the tunable bandgap energy (Δ) as a function of the applied E -field. Figure 2a data allow a seamless and accurate extraction of the energy gap in thermodynamic equilibrium, using electron transport but without contributions from disorder induced states in the gap^{24,25}. Figure 2c shows the bottom bilayer Δ values in the three samples examined here, as a function of the E -field across the bottom bilayer at the DNP. For comparison we include the theoretical Δ vs. E calculated using a tight-binding self-consistent Hartree approach²¹, which is in very good agreement with the experimental data. Overall, Fig. 2 data provide a comprehensive mapping of the bilayer chemical potential as a function of density and at different E -fields, which in turn allows a seamless extraction of the bandgap energy and effective mass.

We now turn to mapping the chemical potential in bilayer graphene in high magnetic fields, where the technique discussed here can be used to investigate Landau level (LL) energies. Figure 3a shows the longitudinal resistivity (ρ_{xx}) measured as a function of V_{BG} and V_{TL} in a perpendicular magnetic field $B = 14$ T, in sample #1. The clear ρ_{xx} minima evince quantum Hall states (QHSs) at all integer filling factors (ν) up to $\nu = 15$; the $\nu = 0$ QHS is marked by a ρ_{xx} maximum. The four fold, spin and valley LL degeneracy is lifted thanks to interaction-enhanced

Zeeman splitting⁶, and the electric field induced layer (valley) degeneracy lifting³⁻⁵. Interestingly, examination of Fig. 3a data shows that the QHSs stabilized by the spin and valley degeneracy lifting, i.e. $\nu \neq \pm 4, 8, 12$, etc..., undergo transitions at finite E -field values as a result of the interplay between the LL spin and valley splitting. Specifically, the $\nu = 1, 3, 5, 7, 9, 11$ (odd filling) QHSs are absent at $E = 0$ and emerge as an E -field is applied. On the other hand the half fillings $\nu = 0, 6, 10$ of the spin and valley degenerate LL are present at $E = 0$ and undergo transitions at finite E -field values.

Figure 3b data, a magnified view of dashed rectangle in Fig. 3a, allow a closer inspection of the $N = 0$ and $N = 1$ QHSs and their phase transitions with the transverse E -field. These data show strong $\nu = 0$ QHS at $E = 0$, as well as at high E -field, marked by diverging ρ_{xx} values, consistent with previous experimental reports^{18,19}. Theoretical considerations^{7,8}, substantiated by recent experimental data²⁶ indicate that the insulating $\nu = 0$ QHS in the proximity of $E = 0$ is described by a canted antiferromagnetic ground state, where electrons in different valleys have opposite in-plane spin orientation and a net out-of-plane spin polarization, while the $\nu = 0$ state at high E -field is valley (layer) polarized. Surprisingly, as a function of E -field the insulating ρ_{xx} at $\nu = 0$ collapses at *two* distinct E -field values, rather than one^{18,19}, indicating two distinct transitions and the observation of a new phase in between the canted antiferromagnetic and layer-polarized phases.



The QHS transitions evinced by Fig. 3a and 3b data can be qualitatively understood using the single-electron LL energy diagram of Fig. 3c. In this picture the $N = 0$ and $N = 1$ LL energies have a different dependence on the E -field, in agreement with tight-binding theoretical considerations³, which in turn explain the two distinct transitions at $\nu = 0$, as well as the emergence of $\nu = \pm 1$ and ± 3 QHS at finite E -field. Theoretical considerations⁹ which include the electron-electron interaction using a Hartree-Fock formalism suggest a more subtle origin for the $N = 0, 1$ QHSs. In this picture, the intermediate $\nu = 0$ QHS between the canted antiferromagnetic and layer-polarized phases is a spin-layer coherent phase, where LLs with the same orbital index but different spin and valley degrees of freedom, e.g. solid red (orange) and dashed dark (light) blue in Fig. 3c form coherent superpositions. In the single-particle picture of Fig. 3c, at $\nu = 0$ electrons in the $N = 0$, spin down, top layer LL (solid red line in Fig. 3c) should move to the $N = 0$, spin up, bottom layer LL (dashed dark blue in Fig. 3c) at a finite E -field by changing both spin and valley orientations, while retaining the orbital index. In the many-body picture however, electrons favor a coherent superposition of the two states at the transition between the two incoherent canted antiferromagnetic and layer-polarized phases.

The interplay between the spin splitting and the E -field induced valley (layer) splitting at $N = 2$ depicted in Fig. 3c explains the absence of $\nu = -5$ and -7 QHSs at $E = 0$, their emergence with the applied E -field, as well as the phase transition at $\nu = -6$ at a finite E -field (Fig. 3a). Similar transitions are observed at $\nu = -10$ and -14 QHSs. A noteworthy exception from this single-particle picture is the evolution of the $\nu = \pm 2$ QHSs, which are present at $E = 0$, vanish at a relatively small E -field, and then reemerge (Fig. 3b). This observation can be explained within the theoretical framework of ref. 9. The $\nu = \pm 2$ at $E = 0$ is a layer-coherent QHS, where the LLs with the same orbital index and spin orientation but different layer (valley) degrees of freedom,

e.g. dashed red (orange) and dashed dark (light) blue LLs of Fig. 3c form a coherent superposition thanks to the exchange interaction. At a finite E -field the different on-site energies in different layers lead to an incoherent $\nu = \pm 2$ phase with a zero in-plane and a net out-of-plane spin polarizations.

Figure 3d summarizes the critical E -field values at which half filled LL QHSs undergo the phase transitions discussed above, as a function of B -field and for different LL indices determined from the transitions of $\nu = 0, 6, 10, 14$ QHSs. The E -field values are calculated using Eq. (3), and including the layer Fermi energies, which will be addressed in more detail in Fig. 4. Because the $N = 0, 1$ LL wavefunctions in different valleys are fully layer polarized³ we can use for comparison the internal electric field in a layer polarized $\nu = 0$ QHS, $E_{int} = 4(e^2 B/h)/2\epsilon_0$ (dashed line in Fig. 3d)¹⁹. The data of Fig. 3 show that the critical E -field values at which the LLs become layer polarized are comparable to E_{int} for $N = 0$ and $N = 1$, and increase for higher N . This observation is consistent with higher LL wavefunctions have a reduced layer polarization by comparison to $N = 0, 1$ ⁴.

The chemical potential mapping discussed above allows us to determine the LL energies in bilayer graphene as a function of filling factor and magnetic field. Figure 4a shows a contour plot of the bottom bilayer ρ_{xx} as a function of V_{BG} and V_{TL} , measured at $B = 12$ T, with the top bilayer charge neutrality line transposed on the contour plot (white line). Note that the transverse E -field across the bottom bilayer at DNP is 0.54 and 0.21 V/nm for sample #1 and #2 respectively, values higher than the $N = 0, 1$ LL critical E -field. Therefore along the top layer charge neutrality line, the bottom bilayer $\nu = 0$ QHS is layer polarized. At each integer filling of the bottom bilayer the top graphene neutrality line displays an abrupt change in the V_{TL} value, which translates into a chemical potential jump of bottom bilayer in units of eV. The sharp staircases-

like discontinuity particularly at the bottom bilayer $\nu = 0, -4, -8, -12, -16$ QHSs testifies to a reduced LL broadening, which contrasts previous measurement in double monolayer heterostructures using metal-oxide as interlayer dielectric¹⁶.

Figure 4b represents the LL orbital energies as a function of B -field and for LL index, determined from the chemical potential at the half filling of each LL orbital index, namely $\nu = 6, 10, 14$, corresponding to $N = 2, 3, 4$, respectively. The LL orbital energies increase linearly with magnetic field, consistent with the theoretical $\mu = \hbar\omega_c\sqrt{N(N-1)}$ dependence³; here $\omega_c = eB/m^*$ is the cyclotron frequency, and m^* the effective mass. The inset of Fig. 4b shows the m^* vs. N dependence determined from the slope of μ vs. B at each LL. The effective mass increases with the LL index, similar to the m^* vs. n dependence observed at $B = 0$ T (Fig. 2b).

Interestingly, a closer look at the chemical potential of $N = 0, 1$ LL, shown in Fig. 4a inset and Fig. 4c, reveals chemical potential jumps at integer fillings $\nu = 2, 0, -1, -2$, and -3 , as well as a *decreasing* chemical potential vs. filling factor (density) in the proximity of the QHSs stabilized in the $N = 0, 1$ LLs. The decreasing μ vs. n dependence observed in the proximity of QHSs, while counter-intuitive in a single particle picture stems from a strong exchange interaction, and translates into a negative compressibility of the electron system²⁷. A similar observation has been reported in monolayer graphene, where the chemical potential was probed through capacitance measurements²⁸. Using the chemical potential jump at integer fillings, we determine the broken symmetry QHS gaps (Δ_ν) at filling factors $\nu = -3, -2, -1, 0, 2$, as a function of B -field, as shown in Fig. 4d. We note that our method to quantify the gap is different from the activation energies determined from the resistivity temperature dependence^{29,30}, which tends to underestimate the gaps, and is similar to spectroscopic techniques through scanning single-electron transistor¹³, scanning probe microscopy³¹, or capacitance measurements²⁸. However,

unlike these latter techniques the measurement discussed here allows control of both density and transverse electric field in the electron system investigated.

Figure 4d data show that the $\nu = 0$ gap in samples #1, #2 is independent on B -field. While these observations maybe appear to contrast the linear B -field dependence of the $\nu = 0$ gap observed in single-gated bilayer graphene^{13,30}, we note that Fig. 4d data represent the $\nu = 0$ gap in the layer polarized phase, while ref. 13 and 30 probe the $\nu = 0$ gap in the spin-polarized (canted anti-ferromagnet) phase. The layer polarized $\nu = 0$ gap is controlled by the interaction, Zeeman splitting, as well as the E -field induced on-site energy difference. At moderate E -fields the competition between the single particle splitting, which decreases with the B -field, and the $\propto \sqrt{B}$ interaction term leads to a Δ_0 weakly dependent on the applied B -field⁹, consistent with Fig. 4d data.

Examination of Fig. 4d data reveals several noteworthy observations. The gaps of $\nu = -3, -1, \pm 2$ have a linear dependence on the B -field, a trend similar to results obtained in single-gated suspended bilayer graphene¹³, and probed in the spin-polarized phase. While theoretical considerations^{6, 9} suggest a sublinear B -field dependence associated with the $\propto \sqrt{B}$ of the interaction energy, the non-linearity is weak particularly in the B -field range probed here. Furthermore, the broken symmetry QHSs observed in the $N = 0, 1$ LLs show a marked electron-hole asymmetry. Specifically, Δ_1 is higher than Δ_2 for both samples #1 and #2, while $\nu = -1$ and -3 have gaps larger than those of $\nu = 1$ and 3 , which are too small to be resolved experimentally. The electron-hole asymmetry observed experimentally is consistent with a detailed Hartree-Fock analysis⁹ of the broken symmetry QHSs of the $N = 0, 1$ LLs.

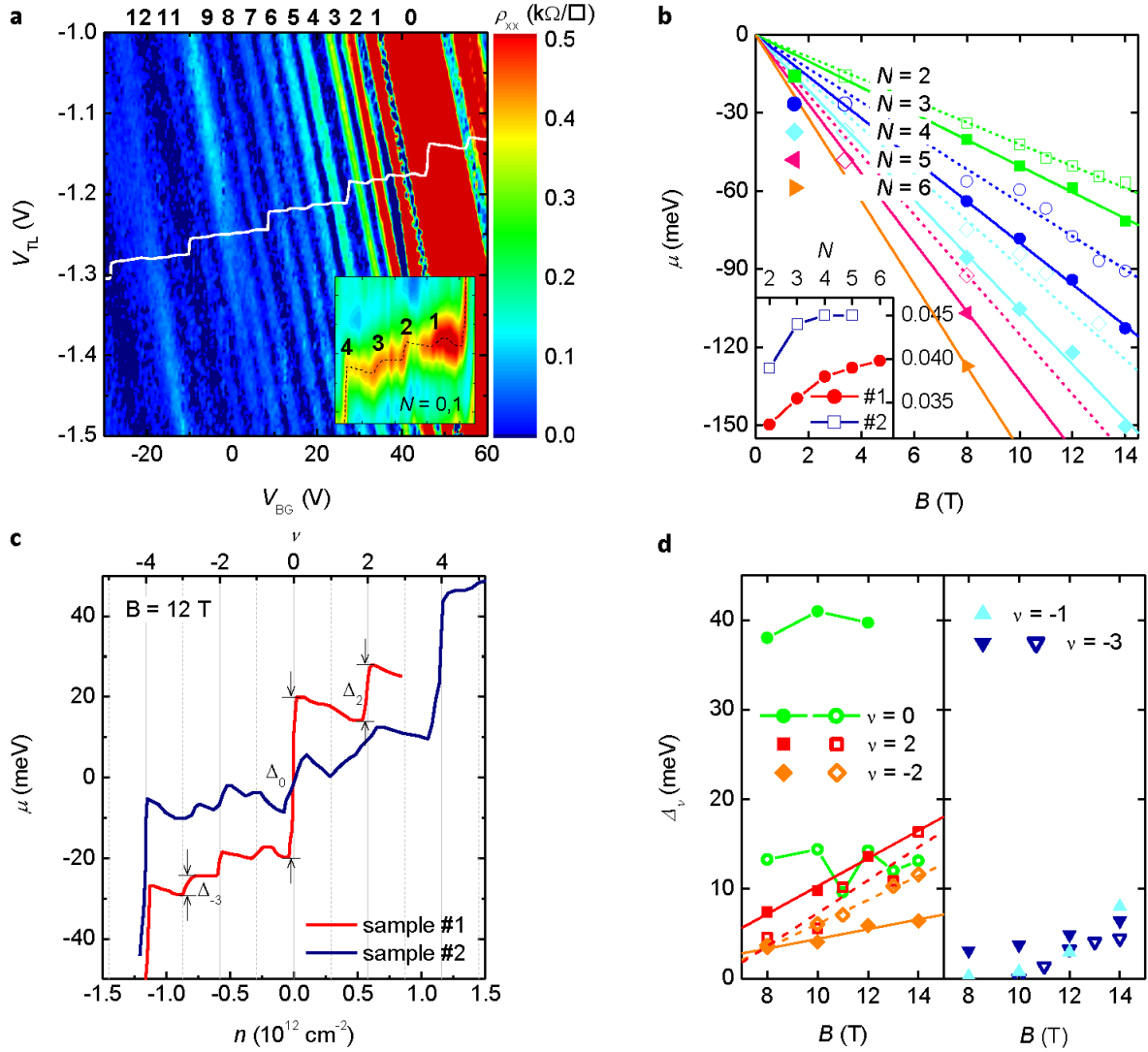


Figure 4. Landau level energies and broken symmetry gaps in bilayer graphene. (a) Contour plot of the bottom layer resistivity ρ_{xx} as a function of V_{TL} and V_{BG} measured at $B = 12$ T and $T = 1.5$ K in sample #1, along with the top layer charge neutrality locus (white line) transposed on the contour plot. The top axis shows the QHS filling factors. The inset shows the top layer resistivity ρ_{xx} as a function of V_{TL} and V_{BG} , as the top layer charge neutrality line crosses the $\nu = 0, -1, -2, -3, -4$ QHS states (hole side of $N = 0, 1$ LLs) of the bottom layer. Each crossing is marked by a distinct jump. (b) Orbital LL energies as a function of B -field and LL index in samples #1 (filled symbols) and #2 (open symbols), determined from the chemical potential at the half filling of each LL orbital index. The inset shows the m^* values vs. N extracted from the main panel data in samples #1 and #2. (c) Bottom bilayer μ vs. n (bottom axis) and ν (top axis), measured at $B = 12$ T. The data reveals marked jumps associated with each broken symmetry QHS, as well as negative compressibility in the proximity of QHSs. (d) Measured QHSs gaps at $\nu = 2, 0, -1, -2, -3$ in sample #1 (filled symbols) and #2 (open symbols).

This study also suggests Δ_2 (Δ_2) to increase (decrease) with an applied E -field, in agreement with Fig. 4d data which show Δ_2 (Δ_2) is larger (smaller) in sample #1 with respect to sample #2. We note however that the QHS gap values of Fig. 4d are all smaller than the theoretical calculations, a common thread in Hartree-Fock calculations.

In summary we present a comprehensive study of the chemical potential and quantum Hall ferromagnetism in bilayer graphene using double bilayer heterostructures. By using the top layer as a resistively detected Kelvin probe we map the chemical potential in zero and high magnetic fields. The chemical potential vs. density dependence is strongly non-linear, allows a seamless extraction of the transverse electric field-induced band gap, as well as the quantum Hall state gaps. The quantum Hall data reveal spin-to-valley polarized transitions in all orbital Landau levels, as well as new phases at filling factors $\nu = 0$ and $\nu = \pm 2$, theoretically predicted to have coherent superpositions between LLs.

Methods

The fabrication of samples investigated here starts with consecutive mechanical exfoliations of hBN onto silicon dioxide thermally grown on a highly doped Si substrate, and bilayer graphene flakes onto PMMA layer on a water-soluble polyvinyl alcohol (PVA). AFM was performed on hBN to determine the thickness, and probe the surface topography, and optical contrast and Raman spectroscopy were used to identify the number of graphene layers. The bilayer graphene layer was transferred on top of the hBN using the dry-transfer and alignment methods similar to those described in ref. 14 and 15. Electron-beam lithography and oxygen plasma etching were performed to define a multi-terminal Hall bar. The second, relatively thin hBN crystal and the topmost bilayer graphene were successively transferred on top of the Hall bar, and the top graphene was patterned into a multi-terminal Hall bar. An etch-through of the

top and bottom graphene layers ensures the Hall bar edges are aligned. After the transfer of each layer, ultra high vacuum annealing at either 350 °C or 320 °C was performed to remove process residue. The electrical transport measurement was performed using small signal, low frequency lock-in techniques, in a variable-temperature liquid ^4He flow cryostat. A radio frequency transformer is used to flow AC currents in a given layer, while applying a DC bias with respect to ground.

References

1. Novoselov, K. S. *et al.* Unconventional quantum Hall effect and Berry's phase of 2π in bilayer graphene. *Nature Phys.* **2**, 177–180 (2006).
2. Castro Neto, A. H., Guinea, F., Peres, N. M. R., Novoselov, K. S. & Geim, A. K. The electronic properties of graphene. *Rev. Mod. Phys.* **81**, 109–162 (2009).
3. McCann, E. & Fal'ko, V. I. Landau-level degeneracy and quantum Hall effect in a graphite bilayer. *Phys. Rev. Lett.* **96**, 086805 (2006).
4. Castro, E. V. *et al.* Biased bilayer graphene: Semiconductor with a gap tunable by the electric field effect. *Phys. Rev. Lett.* **99**, 216802 (2007).
5. Nakamura, M., Castro, E. V., Dora, B. Valley Symmetry Breaking in Bilayer Graphene: A Test of the Minimal Model. *Phys. Rev. Lett.* **103**, 266804 (2009).
6. Barlas, Y., Côté, R., Nomura, K. & MacDonald, A. H. Intra-Landau-level cyclotron resonance in bilayer graphene. *Phys. Rev. Lett.* **101**, 097601 (2008).
7. Kharitonov, M. Edge excitations of the canted antiferromagnetic phase of the $\nu = 0$ quantum Hall state in graphene: A simplified analysis. *Phys. Rev. B* **86**, 075450 (2012).
8. Kharitonov, M. Canted antiferromagnetic phase of the $\nu = 0$ quantum Hall state in bilayer graphene. *Phys. Rev. Lett.* **109**, 046803 (2012).

9. Lambert, J. & Côté, R. Quantum Hall ferromagnetic phases in the Landau level $N = 0$ of a graphene bilayer. *Phys. Rev. B* **87**, 115415 (2013).
10. Henriksen, E. A. & Eisenstein, J. P. Measurement of the electronic compressibility of bilayer graphene. *Phys. Rev. B* **82**, 041412(R) (2010).
11. Young, A. F. *et al.* Electronic compressibility of layer-polarized bilayer graphene. *Phys. Rev. B* **85**, 235458 (2012).
12. Rutter, G. M., Jung, S., Klimov, N. N., Newell, D. B., Zhitenev, N. B. & Stroscio, J. A. Microscopic polarization in bilayer graphene. *Nature Phys.* **7**, 649–655 (2011).
13. Martin, J., Feldman, B. E., Weitz, R. T., Allen, M. T. & Yacoby, A. Local compressibility measurements of correlated states in suspended bilayer graphene. *Phys. Rev. Lett.* **105**, 256806 (2010).
14. Dean, C. R. *et al.* Boron nitride substrates for high-quality graphene electronics. *Nature Nanotechnol.* **5**, 722–726 (2010).
15. Dean, C. R. *et al.* Multicomponent fractional quantum Hall effect in graphene. *Nature Phys.* **7**, 693–696 (2011).
16. Kim, S. *et al.* Direct measurement of the Fermi energy in graphene using a double-layer heterostructure. *Phys. Rev. Lett.* **108**, 116404 (2012).
17. Oostinga, J. B., Heersche, H. B., Liu, X. L., Morpurgo, A. F. & Vandersypen, L. M. K. Gate-induced insulating state in bilayer graphene devices. *Nature Mater.* **7**, 151–157 (2008).
18. Weitz, R. T., Allen, M. T., Feldman, B. E., Martin, J. & Yacoby, A. Broken symmetry states in doubly gated suspended bilayer graphene. *Science* **330**, 812–816 (2010).
19. Kim, S., Lee, K. & Tutuc, E. Spin-polarized to valley-polarized transition in graphene bilayers at $\nu = 0$ in high magnetic fields. *Phys. Rev. Lett.* **107**, 016803 (2011).

20. Zou, K., Hong, X. & Zhu, J. Effective mass of electrons and holes in bilayer graphene: Electron-hole asymmetry and electron-electron interaction. *Phys. Rev. B* **84**, 085408 (2011).
21. Min, H. K., Sahu, B., Banerjee, S. K. & MacDonald, A. H. Ab initio theory of gate induced gaps in graphene bilayers. *Phys. Rev. B* **75**, 155115 (2007).
22. Kane, C. L. & Mele, E. J. Electron interactions and scaling relations for optical excitations in carbon nanotubes. *Phys. Rev. Lett.* **93**, 197402 (2004).
23. Borghi, G., Polini, M., Asgari, R. & MacDonald, A. H. Compressibility of the electron gas in bilayer graphene. *Phys. Rev. B* **82**, 155403 (2010).
24. Zou, K., Zhu, J. Transport in gapped bilayer graphene: The role of potential fluctuations. *Phys. Rev. B* **82**, 081407(R) (2010).
25. Taychatanapat, T. & Jarillo-Herrero, P. Electronic transport in dual-gated bilayer graphene at large displacement fields. *Phys. Rev. Lett.* **105**, 166601 (2010).
26. Maher, P. *et al.* Evidence for a spin phase transition at charge neutrality in bilayer graphene. *Nature Phys.* **9**, 154–158 (2013).
27. Eisenstein, J. P., Pfeiffer, L. N. & West, K. W. Compressibility of the two-dimensional electron gas: Measurements of the zero-field exchange energy and fractional quantum Hall gap. *Phys. Rev. B* **50**, 1760–1778 (1994).
28. Yu, G. L. *et al.* Interaction phenomena in graphene seen through quantum capacitance. *PNAS* **110**, 3282–3286 (2013).
29. Zhao, Y., Cadden-Zimansky, P., Jiang, Z. & Kim, P. Symmetry breaking in the zero-energy Landau level in bilayer graphene. *Phys. Rev. Lett.* **104**, 066801 (2010).
30. Feldman, B. E., Martin, J. & Yacoby, A. Broken-symmetry states and divergent resistance in suspended bilayer graphene. *Nature Phys.* **5**, 889–893 (2009).

31. Song, Y. J. *et al.* High-resolution tunneling spectroscopy of a graphene quartet. *Nature* **467**, 185–189 (2010).

Acknowledgements

This work was supported by ONR, NRI SWAN, and Intel. We thank D. C. Dillen and K. Kim for technical support, and A. H. MacDonald, P. Kim, and F. Ghahari for discussions.